Science Advances

AAAS

Supplementary Materials for

Discovery of Lorentz-violating type II Weyl fermions in LaAlGe

Su-Yang Xu, Nasser Alidoust, Guoqing Chang, Hong Lu, Bahadur Singh, Ilya Belopolski,
Daniel S. Sanchez, Xiao Zhang, Guang Bian, Hao Zheng, Marious-Adrian Husanu, Yi Bian,
Shin-Ming Huang, Chuang-Han Hsu, Tay-Rong Chang, Horng-Tay Jeng, Arun Bansil, Titus Neupert,
Vladimir N. Strocov, Hsin Lin, Shuang Jia, M. Zahid Hasan

This PDF file includes:

section S1. Additional methods

In figs. S1 to S3, we show basic characterizations of our LaAlGe samples. Energy dispersive X-ray spectroscopy measurements shown in fig. S1 provides a quantitative measure of the chemical composition of our LaAlGe. Through this data, we conclude (*1*) that our samples indeed consists of the three elements, La, Al, and Ge and (*2*) that the chemical composition is La:Al:Ge = 1:1:1. The X-ray diffraction data shown in fig. S2 confirm the crystal structure reported by previous diffraction experiments (41⁻43) and determine the following lattice constants, $a = b = 4.336\ A$ and $c = 14.828\ A$, also consistent with data from the previous reports (41⁻43). Finally, the low-energy electron diffraction data (LEED) shown in fig. S3 shows a clear 4-fold symmetry, which shows that there is no surface reconstruction. In fact, quantitatively, a surface reconstruction (e.g. 2×1) would change the surface Brillouin zone size for the surface state. Here, we have measured the bulk band structure via soft-X-ray ARPES and the surface band structure via low-photon-energy ARPES. The bulk band structure data match the bulk BZ size while the surface data also match the surface BZ size. Therefore, our ARPES measurements quantitatively exclude the possibility of a surface reconstruction.

table S1. Energy dispersive spectroscopy (EDS) data.

Element	Edge	Apparent concentration	k ration	Weight (wt%)	Atomic ratio	Ref. compound
Al	K	3.76	0.03403	11.83	33.28	Al_2O_3
Ge	K	39.07	0.39071	31.34	33.74	Ge
La	L	74.96	0.67255	56.83	32.97	LaB_6
Total				100	100	

In fig. S4, we further explain the distribution of Weyl nodes in LaAlGe. We see that (S4A) all the W_1 and $W_3'(W_3'')$ nodes are located at the $k_z = 0$ plane whereas the W_2 nodes are at finite k_z values. Figure. S4B shows the $k_z = W_2$ plane only. There are 8 W_2 Weyl nodes per $k_z = W_2$ plane and there are two such planes in the bulk BZ (fig. S4A). Hence there are 16 W_2 Weyl nodes in total. Figure S4C shows the $k_z = 0$ plane only. The W_1 Weyl nodes are located near the BZ boundaries. There are 8 W_1 Weyl nodes. The W_3' and W_3'' Weyl nodes are located near the 45° lines of the $k_z = 0$ plane. There are 8 W_3' nodes and 8 W_3'' nodes. Therefore, the total number of Weyl nodes is 8 (W_1) + 16 (W_2) + 8 (W_3') + 8 (W_3'') = 40.
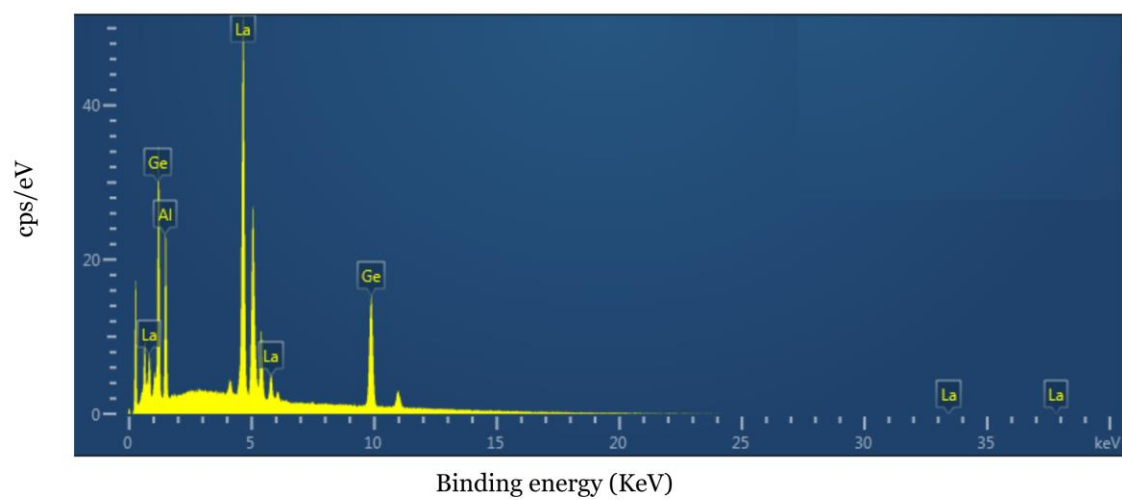
fig. S1. Energy-dispersive x-ray spectroscopy of LaAlGe samples. Cps stands for counts per second.
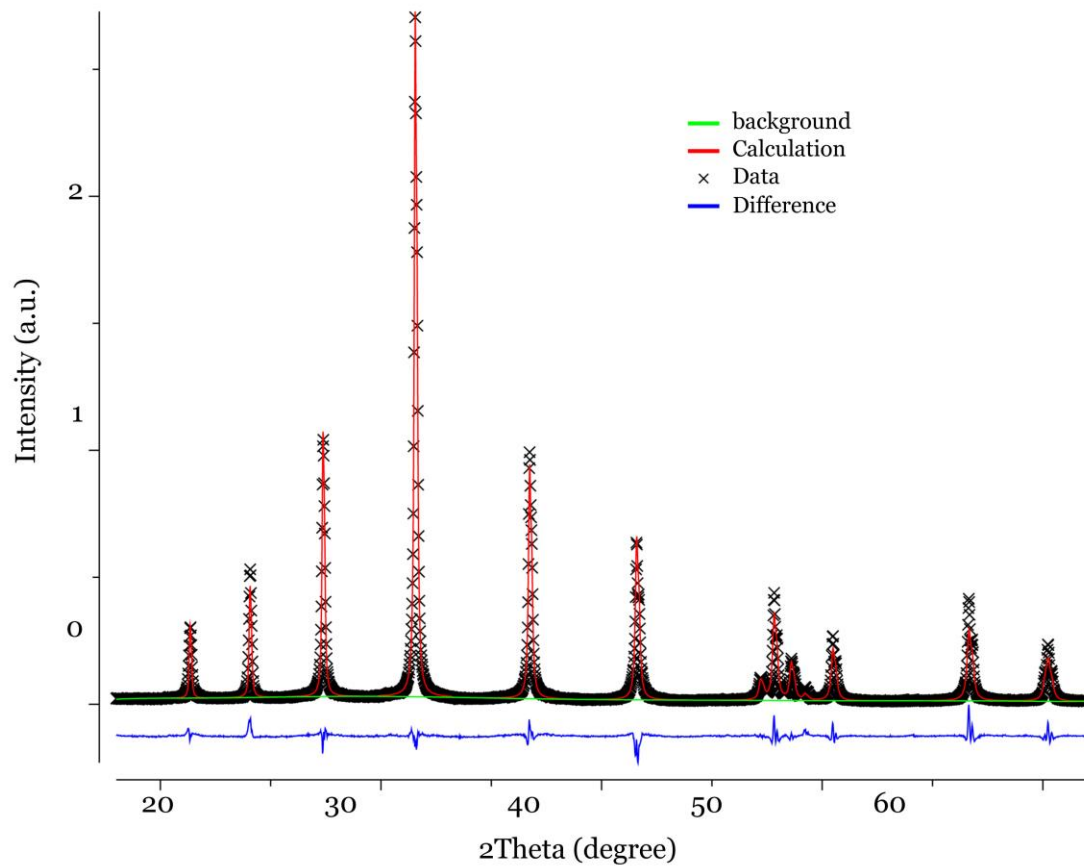
fig. S2. XRD data of LaAlGe. (**A**) Our XRD measurements confirm the crystal structure reported by previous diffraction experiments (41‑43) and determine the following lattice constants, $a = b = 4.336\,A$ and $c = 14.828\,A$, also consistent with data from the previous reports (41‑43).
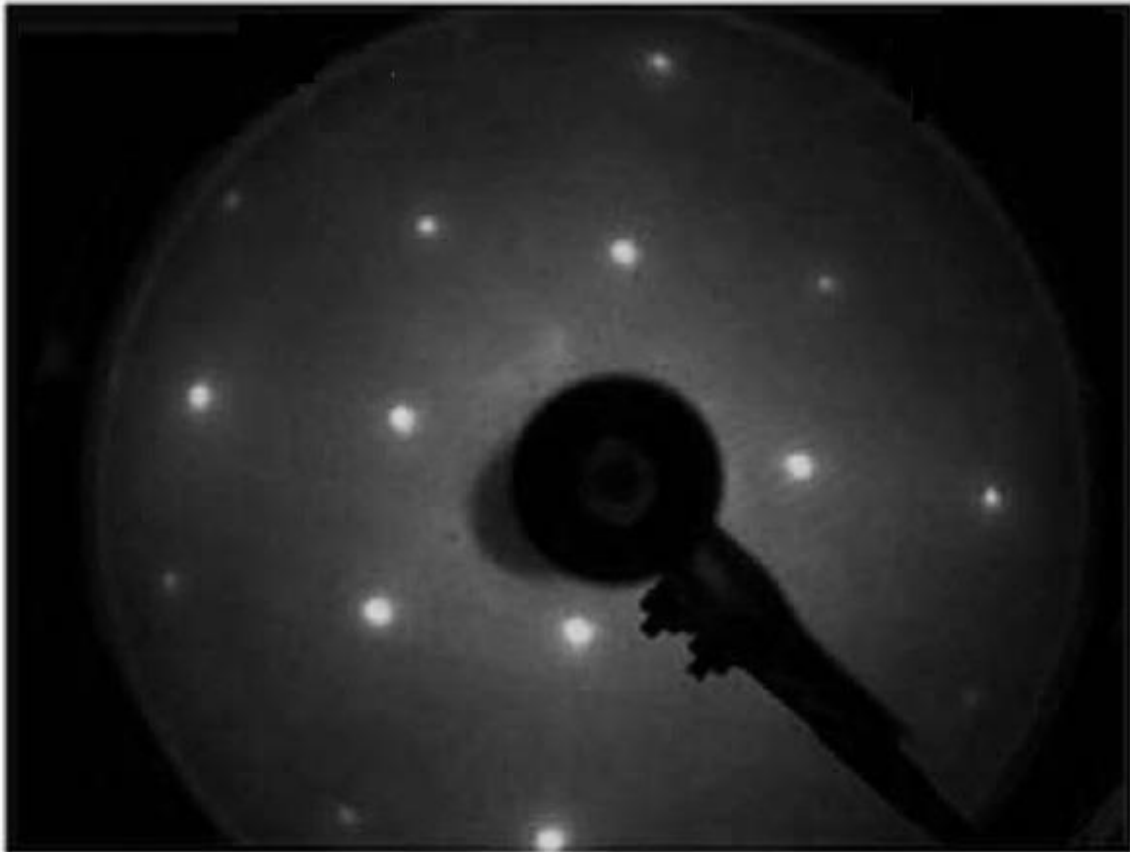
fig. S3. Low-energy electron diffraction data of LaAlGe taken at 100-eV electron energy.

The observed 4-fold symmetry excludes the existence of surface reconstructions.
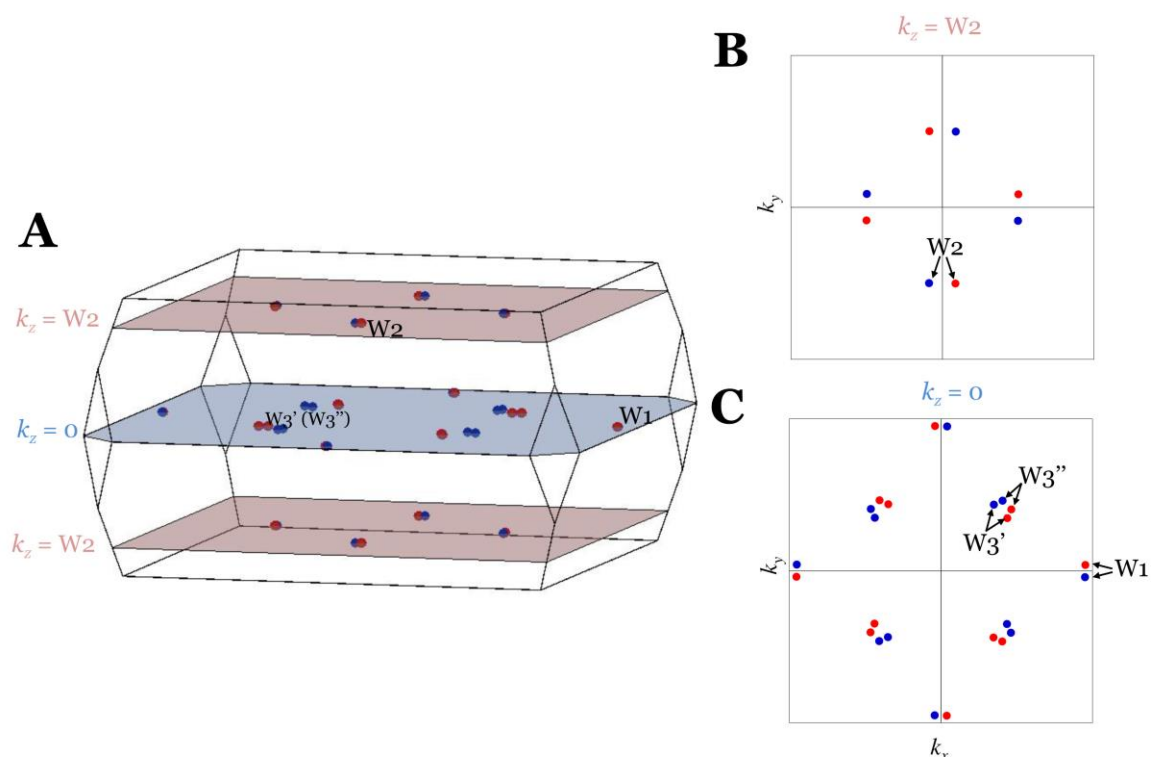
fig. S4. The 40 Weyl nodes in LaAlGe.

section S2. Full characterization of the type II Weyl fermions in LaAlGe

Based on our data and calculations, we can fully characterize the Weyl fermions observed in LaAlGe. This can help us quantify the amount of Lorentz symmetry breaking, and deduce all the information about the Weyl Hamiltonian including the magnitude of the Berry curvature. In order to do so, we need to obtain the Fermi velocities of the two bands that form the Weyl cone along the following momentum space directions, (100), (010), (001), (110), (101), and (011).

table S2. ARPES-measured Fermi velocities near W_2. Currently, we do not have data that can be used along the (101) direction.

Direction	(100)	(010)	(001)	(110)	(101)	(011)
ARPES v_+ (eVÅ)	1.85	-0.52	0.67	0.44	N.A.	0.21
ARPES v_- (eVÅ)	-1.22	-2.89	-1.27	-2.59	N.A.	-2.65

table S3. Calculated Fermi velocities near W_2.

Direction	(100)	(010)	(001)	(110)	(101)	(011)
ARPES v_+ (eVÅ)	1.54	-0.39	0.43	0.35	0.96	0.01
ARPES v_- (eVÅ)	-1.26	-2.65	-1.36	-2.69	-1.82	-2.82

We want to compute the numerical values entering the 3-vector $\boldsymbol{v}$ and the symmetric and positive definite 3×3 matrix $\widehat{\boldsymbol{U}}$

$$\boldsymbol{v} = (v_1, v_2, v_3)^T, \quad \widehat{\boldsymbol{U}} = \begin{pmatrix} u_1 & w_3 & w_2 \\ w_3 & u_2 & w_1 \\ w_2 & w_1 & u_3 \end{pmatrix}$$

that determine the dispersion $\epsilon(\boldsymbol{k}) = \boldsymbol{k}^T \boldsymbol{v} \pm \sqrt{\boldsymbol{k}^T \widehat{\boldsymbol{U}} \boldsymbol{k}}$ near the Weyl node.

From the velocities along the coordinate axes, we find

$$v_1 = \frac{v_{+,(100)} + v_{-,(100)}}{2}, \quad u_1 = \left(\frac{v_{+,(100)} - v_{-,(100)}}{2}\right)^2$$

and similarly for v_2, u_2 and v_3, u_3, as well as

$$w_3 = \frac{1}{8}\left[\left(v_{+,(110)} - v_{-,(110)}\right)^2 - \left(v_{+,(010)} - v_{-,(010)}\right)^2 - \left(v_{+,(100)} - v_{-,(100)}\right)^2\right]$$

and similarly for w_1 and w_2.

We can obtain $\boldsymbol{v}$ and $\widehat{\boldsymbol{U}}$ based on the DFT calculated values in tab.S2

$$\boldsymbol{v}_{\mathrm{DFT}} = (0.14, -1.52, -0.47), \quad \widehat{\boldsymbol{U}}_{\mathrm{DFT}} = \begin{pmatrix} 1.96 & -0.46 & -0.41 \\ -0.46 & 1.28 & -0.04 \\ -0.41 & -0.04 & 0.80 \end{pmatrix}$$

We can also obtain $\boldsymbol{v}$ and $\widehat{\boldsymbol{U}}$ based on the ARPES measured values in Tab. S3, except for w_2, as $v_{\pm,(101)}$ are not available from ARPES data and we used the DFT values instead

$$\boldsymbol{v}_{\mathrm{ARPES}} = (0.32, -1.71, 0.32), \quad \widehat{\boldsymbol{U}}_{\mathrm{ARPES}} = \begin{pmatrix} 2.36 & -0.73 & -0.68 \\ -0.73 & 1.40 & -0.15 \\ -0.68 & -0.15 & 0.94 \end{pmatrix}$$

$\widehat{\boldsymbol{U}}$ should be positive definite. Indeed the eigenvalues are 2.27, 1.15, 0.61 from the DFT calculated results and 2.9036, 1.34784, 0.448551 from the ARPES measured data. However, the matrix $\widehat{\boldsymbol{U}} - \boldsymbol{v}\boldsymbol{v}^T$ is expected to be indefinite. Indeed, it has eigenvalues 2.02, 0.83, -1.36 from the DFT calculated results and 2.46, -1.74, 0.85 from the ARPES measured data. This confirms the type-II nature of the W2 Weyl cone. Moreover, using $\boldsymbol{v}$ and $\widehat{\boldsymbol{U}}$, one can reconstruct the full low-energy dispersion $\epsilon(\boldsymbol{k}) = \boldsymbol{k}^T\boldsymbol{v} \pm \sqrt{\boldsymbol{k}^T\widehat{\boldsymbol{U}}\boldsymbol{k}}$ as well as the Berry curvature $\Omega(\boldsymbol{k}) = \pm\boldsymbol{k}\det\widehat{\boldsymbol{U}} / \left(\boldsymbol{k}^T\widehat{\boldsymbol{U}}\boldsymbol{k}\right)^{3/2}$. (Only the sign $\pm$ of the Berry curvature cannot be determined, as the spectroscopic information does not allow to detect whether a Weyl node is a source or a sink of Berry flux.)

section S3. Decisive evidence for type II Weyl fermions

A Weyl semimetal is defined as a material whose low-energy electronic quasi-particle excitations are Weyl fermions. Therefore, to demonstrate the Weyl semimetal state in a material, it is entirely sufficient to observe the bulk Weyl fermion cones. The above statement is correct according to topological band theory. Equally importantly, this has been practiced by a number of important works in the Weyl semimetal field. Specifically, Ref. (*8*) proved the Weyl semimetal state in photonic crystals solely by showing the bulk Weyl fermion data. Similarly, Ref. (*9*) showed the Weyl semimetal state in TaAs solely based on the bulk Weyl fermion data

More importantly, the focus is to show the type-II character in LaAlGe. We emphasize that the distinction between type-I and type-II Weyl fermions solely lies in the bulk Weyl fermion cones. The type-I/type-II character can only be determined by measuring the bulk Weyl cones. This is precisely what we did in this paper. We measured the bulk band structure and directly observed the heavily-tilted bulk Weyl fermion cones. The electronic dispersion of the bulk Weyl cone directly revealed the type-II character of the Weyl fermion cones in LaAlGe. Therefore, our paper presents the most decisive and relevant evidence, which unambiguously proves the type-II Weyl fermion state in LaAlGe.

A Weyl semimetal may also have other hallmarks, including the surface Fermi arcs, a negative longitudinal magneto-resistance due to the chiral anomaly (*11*), a nonlocal transport due to the chiral anomaly (*10*), and a new Fermi arc quantum oscillation (*53*). These other hallmarks including the Fermi arcs are out of the scope and irrelevant to our goal. For example, fig. S5 shows that the surface Fermi arc cannot distinguish between type-I and type-II. As we have emphasized above, the decisive evidence of the type-II character is the bulk Weyl fermion cone band structure. Therefore, it is not required (and often practically very hard) to show all of the other hallmarks of a Weyl node. In fact, none of the Weyl experimental papers have shown all hallmarks to prove the Weyl state. We take an analogy. The topological insulator state like Bi_2Se_3 has many hallmarks including the presence of an odd number of Dirac surface states, the gap opening at the Dirac point by breaking time-reversal symmetry, the topological magneto-electric effect. However, to prove the TI state, nobody has shown all these hall marks. In Bi_2Se_3, which is a topological insulator, the decisive evidence is single Dirac cone at Γ.

A Fermi arcs in a type-I Weyl semimetal

B Fermi arcs in a type-II Weyl semimetal
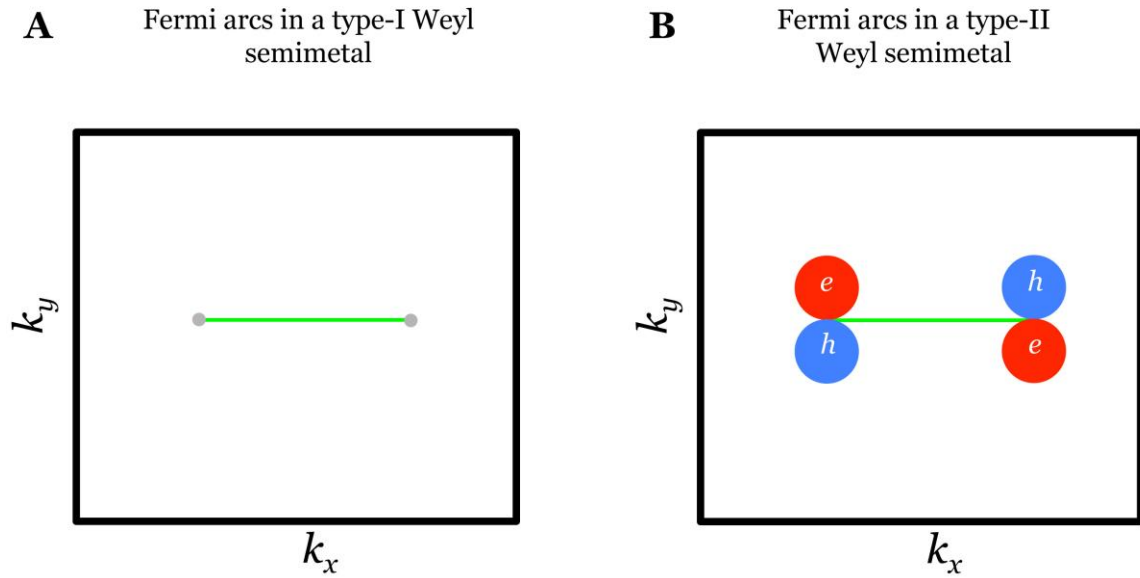
fig. S5. A comparison between the Fermi arcs in type I and type II Weyl semimetals, demonstrating that the Fermi arcs (the green line) cannot be used to discern between type I and type II Weyl fermions. The green line shows the surface Fermi arcs. (**A**) The case for a type-I Weyl semimetal. The grey dots represents the projected pair of type-I Weyl nodes of opposite chirality. (**B**) The case for a type-II Weyl semimetal. Each type-II Weyl node arises from the touching point between an electron and a hole pocket in the bulk, which are represented by the red and blue areas, respectively. It can be seen that the distinction between the type-I and type-II cases solely lies in the bulk Weyl fermions. Therefore, type-I or type-II character can only be determined by measuring the bulk Weyl cone. Showing the Fermi arcs can prove the Weyl semimetal state, but it cannot discern type-I from type-II.

section S4. The importance of measuring the band structure along all three k (k_x, k_y, k_z) directions and the issues in $W_{1-x}Mo_xTe_2$
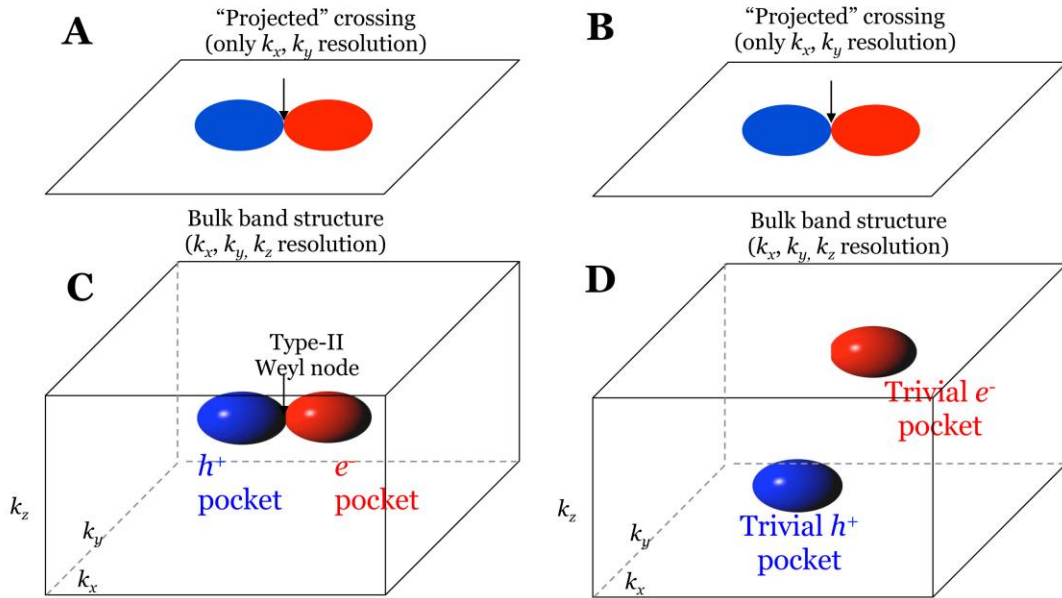
fig. S6. A comparison between a true crossing in the bulk band structure and a "projected" crossing in the projected band structure. (**A**) The Fermi surface of a type-II Weyl semimetal where electron and hole pockets touch to form the type-II Weyl node. On the surface, the projected Fermi surface shows a crossing between the projected electron and hole pockets. On the other hand, in panel (**B**) we have a completely different scenario in the bulk. The electron and hole pockets are totally separated at different k_z values. However, on the surface, their projections can still show a crossing point. This example clearly shows that the observation of a crossing in the projected band structure on surface does not mean a crossing in the bulk. The red and blue ellipsoids represent the electron and hole Fermi surfaces in the bulk Brillouin zone. The red and blue ellipses are the surface projection of the bulk Fermi surfaces.

Since the type-II Weyl fermion node is a touching point in the 3D (bulk) Brillouin zone, it can only be shown by measuring the band structure along all three momentum space directions k_x, k_y and k_z). As emphasized in the main text (fig. S6), probing the projected band structure without k_z resolution cannot demonstrate the existence of a true bulk crossing point in the bulk band structure (a Weyl node).

In this section, we emphasize that this issue is particularly important in the case of the $W_{1-x}Mo_xTe_2$ system because the projected Fermi surface can indeed show ``artifact'' crossings even if the bulk has no Weyl nodes. In fig. S7, we show the band structure of WTe_2 with a lattice constant c = 1.41 nm. As seen in fig. S7**A**, under this lattice constant, WTe_2 is fully gapped without any Weyl node. However, we clearly see projected crossings in the projected Fermi surface (fig. S7**B**), even though the bulk has no Weyl node. To double check the nature of these projected crossings, in fig. S7**C** we show the k_z contribution of the electron and hole pockets in the vicinity of the projected crossings. The different k_z values of the electron and hole pockets again demonstrate that the projected band crossings in this case is not a true crossing in the bulk band structure.
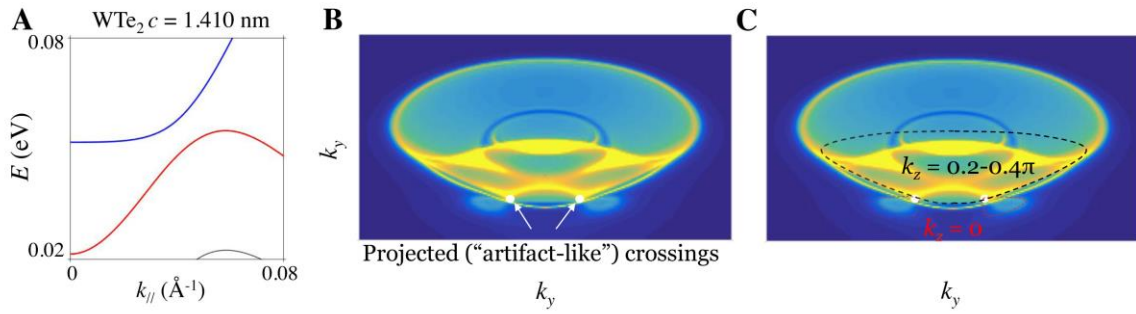
fig. S7. The presence of projected crossing in the projected band structure of WTe₂ even when the bulk has no Weyl nodes. (**A**) The bulk band structure calculation with a lattice constant c = 1.41 nm. Under this lattice constant, WTe₂ is fully gapped without any Weyl node. (**B**) The projected Fermi surface under this condition. Projected crossings are seen between the electron pocket (the big pocket) and the hole pockets (the two little pockets). (**C**) The outer boundary of the hole pockets (red dotted line) arises from the bulk bands at $k_z = 0$ whereas the boundary of the electron pocket marked by the black dotted line arises from bulk bands at $k_z \sim 0.2 - 0.4\,\pi$. The different k_z values of the electron and hole pockets again demonstrate that the projected band crossings in this case is not a true crossing in the bulk band structure.

section S5. Topological definition of Fermi arc surface states and its implications for surface states in LaAlGe and $W_{1-x}Mo_xTe_2$

Below, we will present the following aspects of the Fermi arcs.

(1) The topological definition of Fermi arcs.

(2) How to demonstrate the existence of Fermi arcs in a topological sense.

(3) Why in certain real materials the existence/observability of Fermi arcs becomes ill-defined and why this is the case in LaAlGe.

(4) Why it is less reliable to conclude the existence of Fermi arcs based on a qualitative agreement between calculated and measured surface band structure.

(5) A detailed analysis of the $W_{1-x}Mo_xTe_2$ ARPES papers: Why these papers do not experimentally demonstrate the type-II Weyl fermions.

(1) The topological definition of Fermi arcs.

Definition I: The literal definition of a topological Fermi arc is a surface state that is terminated onto the projection of a Weyl node (fig. S8**A**).

Definition II: An equivalent definition that reveals the topological nature more explicitly can be described as the following: If one draws a closed loop in the surface Brillouin zone (fig. S8**A**), the existence of a chiral edge mode along this loop (fig. S8**B**) defines the existence of a Fermi arc.

We take an intuitive example to explain definition II. As shown in fig. S8**A**, we have a pair of projected Weyl nodes and a Fermi arc connecting them. We draw a 1D closed k loop as shown by the dotted circle. We will show the following:

The number of chiral edge modes along the loop $=$ The number of surface Fermi arcs.

Here comes the proof:

We first prove:

the number of chiral edge modes $\rightarrow$ the number of surface Fermi arcs.

Assuming no knowledge on the existence of Fermi arcs, we only know that there is one chiral edge state along the closed k loop as shown in fig. S8**B**. This band structure in fig. S8**B** is the same as the edge band structure of a quantum Hall system with a Chern number of +1. We know

that this closed k loop corresponds to the projection of a cylindrical pipe that crosses the bulk Brillouin zone along the k_z direction (fig. S8**B**). Hence, we know that the Chern number of the bulk band structure on the cylindrical pipe is +1. Therefore, we know that the cylindrical pipe must encloses a Berry curvature monopole, i.e., a Weyl node, with a chiral charge of +1. Hence, on the surface, the closed k loop encloses a projected Weyl node with a Chiral charge of +1. As a result, we know that the surface state (the green line) is a Fermi arc.
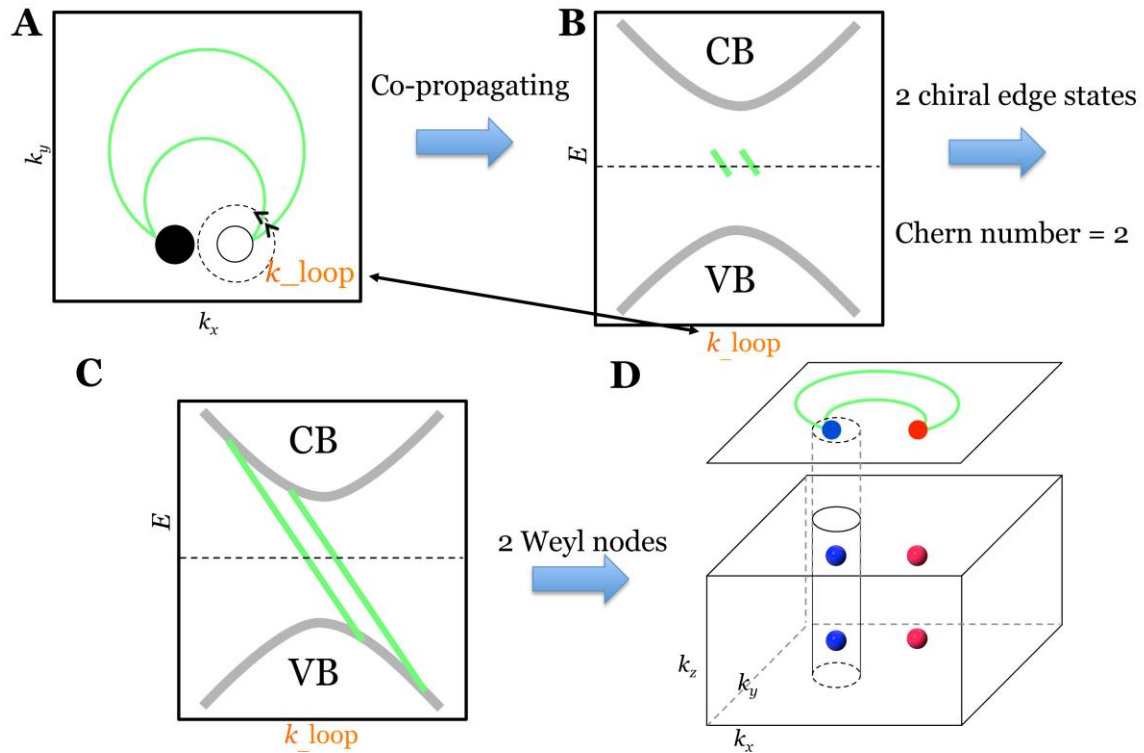
fig. S8. Definition of the topological Fermi arc surface states. (**A**) A surface Brillouin zone with two projected Weyl nodes and a surface Fermi arc connecting the two nodes. The black and white dots represent the two projected Weyl nodes with a projected chiral charge of ± 1. The green line represents the surface Fermi arc. The dotted circle is a closed k loop in the surface BZ that encloses a projected Weyl node with +1 chiral charge. (**B**) The surface band structure along the closed k loop as shown by the dotted circle in panel (A). (**C**) The closed k loop on the surface corresponds to a cylindrical pipe that goes across the bulk BZ along the k_z direction. Because the cylindrical pipe encloses the Weyl node, the bulk band structure on this pipe has a Chen number of +1. Therefore, the closed k loop on the surface, which is the projection of the pipe, has one chiral edge state. This justifies the band structure along the loop shown in panel (B).

We also prove the reverse logic:

the number of surface Fermi arcs → the number of chiral edge modes.

Now we assume that we know that the green line surface state is a Fermi arc, and we want to prove that the surface band structure along the closed k loop will show as a chiral edge mode. Because the green line is a Fermi arc, its termination points (the black and white dots in fig. S8**A**) are two projected Weyl nodes. The closed k loop (the dotted circle in fig. S8**A**) on the surface, which corresponds to the projection of a cylindrical pipe in the bulk Brillouin zone (fig. S8**C**), encloses a projected Weyl node. Therefore, the cylindrical pipe encloses a Weyl node of a chiral charge of +1. Hence, the Chern number of the bulk band structure on this pipe is +1. As a result, the band structure along the closed k loop, which is the edge of the pipe, should have one chiral edge state.

The above proof show that ``the number of chiral edge modes along the loop'' and ``the number of surface Fermi arcs'' are equivalent because we can derive one by assuming the other. Hence, we have proved the following:

The number of chiral edge modes along the loop = The number of surface Fermi arcs.
The number of chiral edge modes along the loop = The number of surface Fermi arcs.

(2) How to demonstrate the existence of Fermi arcs in a topological sense.
The topological definitions presented above directly show us the way to demonstrate the existence of Fermi arcs in a topological sense.

Demonstration I: A Fermi arc can be shown by observing a surface state that is directly terminated onto a projected Weyl node (according to definition I).

Demonstration II: The existence of a Fermi arc can be shown by observing a nonzero number of chiral edge modes along a closed k loop in the surface BZ (according to definition II).

(3) Why in certain real materials the existence of Fermi arcs become ill-defined. Why this is the case in LaAlGe.
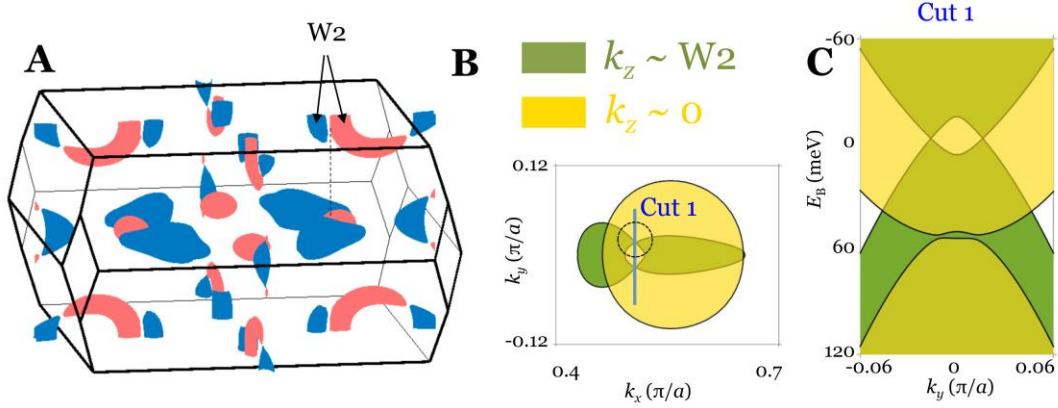
fig. S9. Bulk band structure and its projection onto the surface in LaAlGe. (**A**) ACalculated bulk Fermi surface. The black arrows point to the electron and hole pockets that touch at two discrete points forming a pair of type-II Weyl nodes (W2). The vertical dotted line shows that these pockets forming the W2 Weyl cones are vertically aligned with an irrelevant pocket at $k_z = 0$, the red, pancake-shaped pocket. (**B**) The projected bulk Fermi surface shows that the W2 Weyl nodes are masked by the irrelevant pocket. (**C**) The projected bulk energy dispersion along Cut 1, which is defined by the blue line in panel (B).

We show why the existence of Fermi arcs can be ill-defined. We directly take LaAlGe as the example. The two black arrows in fig. S9**A**, point to the electron and hole pockets that touch at a pair of type-II Weyl nodes (the W2 Weyl nodes). However, there exists an irrelevant trivial pocket at the $k_z = 0$ plane (the red pancake-shaped pocket). As shown by the vertical dotted line in fig. S9, the pair of W2 Weyl nodes and the irrelevant trivial pockets are projected onto the same k region in the surface BZ. Indeed, fig. S9**B** shows the constant energy plot for the projected bulk band structure. We see that the projected W2 Weyl nodes are masked by the irrelevant pocket.

We explain why this condition makes the existence/observability of Fermi arcs in LaAlGe (on the natural cleavage plane) ill-defined.

The literal definition of a topological Fermi arc (a surface state terminated onto the projected Weyl node) becomes inapplicable. A surface state is only well-defined at a (E, k_x, k_y) point where there is no projected bulk state. However, all k points surrounding the Weyl nodes are

masked by the irrelevant pocket. Therefore, the surface state is ill-defined in the vicinity of the node. Therefore, we cannot determine if it is a Fermi arc surface state in this case.

Definition II also becomes inapplicable for the following reasons: We need to first choose a closed k loop that encloses one of the projected Weyl nodes and then show the existence of chiral edge state along the loop. Importantly, this whole argument (Chern number, chiral edge state, and essentially the quantum Hall physics) is based on the assumption that the projected bulk band structure along the chosen k loop has a full energy gap. A chiral edge state is an edge state traversing the band gap. In the absence of a band gap, a chiral edge state is ill-defined. In the case of LaAlGe, fig. S9**C** shows the projected bulk band structure along Cut 1 as defined by the blue line in fig. S9**B**. We see that the energy gap at the k points between the two Weyl nodes is completely masked by the irrelevant pocket. As a result, any closed k loop that encloses only one of the projected W2 Weyl node (e.g., the black dotted circle in fig. S9**B**) will NOT have a full projected gap. Therefore, the existence of Fermi arcs associated with the W2 nodes is ill-defined.

(4) Why it is less reliable to conclude the existence of Fermi arcs based on a qualitative agreement between calculated and measured surface band structure.
We note that the two topological ways of demonstrating Fermi arcs presented above do not depend on the details of the materials and their surface conditions. In other words, these are completely topological arguments.

By contrast, many other ARPES groups have been claiming the observation of Fermi arcs based on a qualitative agreement between theoretically calculated and experimentally measured surface state electronic structures (For example, ARPES papers on $W_{1-x}Mo_xTe_2$ (32‑38)).

We explain why this is not as reliable as the topological arguments presented above:

(a) The details of surface electronic structure depend heavily on the surface conditions. For example, fig. S10 shows the surface Fermi surfaces of the Weyl semimetal TaAs under different surface potentials. It can be seen that the surface Fermi surface varies significantly as a function of surface potential. Therefore, by simply comparing to calculations on features that are not sensitive to the topological nature of the Fermi arcs, one cannot obtain an experimental proof of the Fermi arcs in a topological sense.
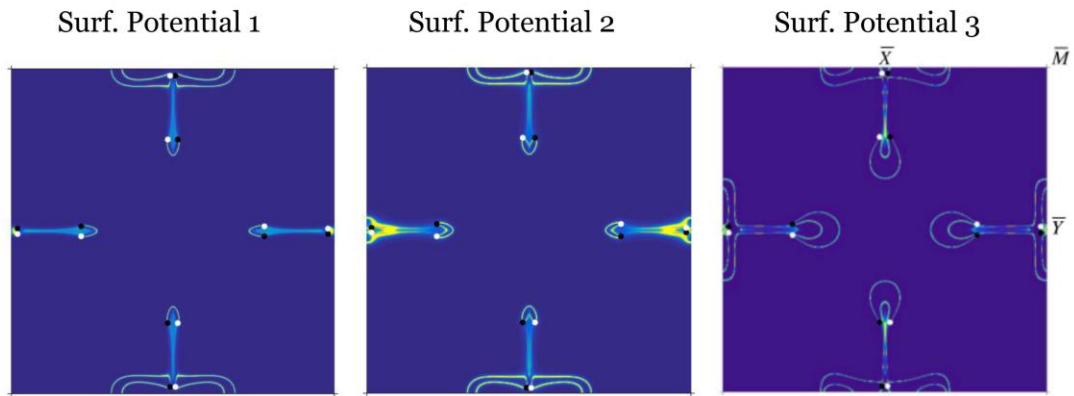
fig. S10. TaAs surface Fermi surface calculations under three different surface onsite potential values. We see that the surface band structure changes dramatically as the surface potential is varied.
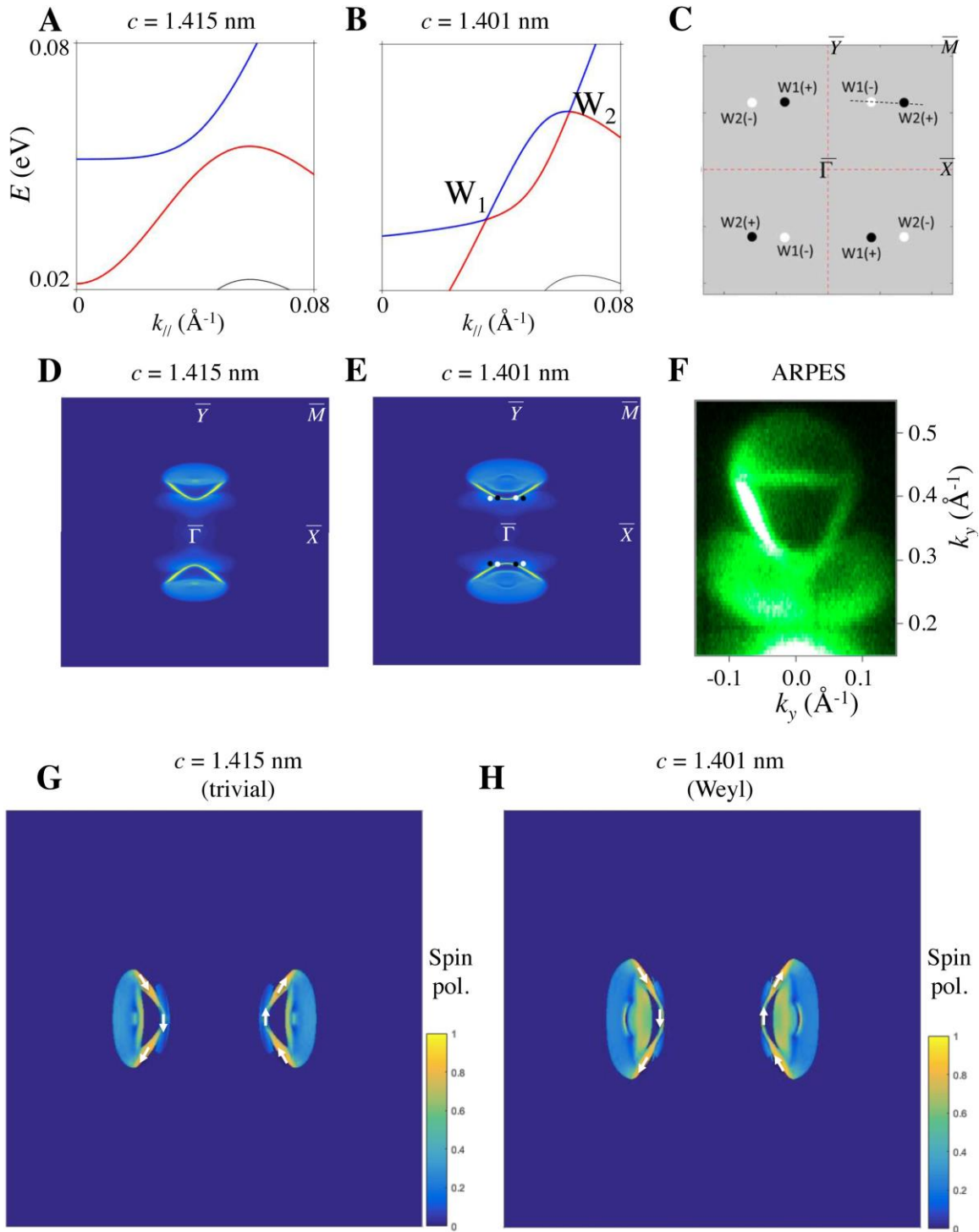
fig. S11. Band structure of WTe₂ under two slightly different lattice constant values. (**A**) Calculated bulk band structure of WTe₂ with the lattice constant reported in Ref. (*54*), c = 1.415 nm. Under this condition, WTe₂ is trivial without no Weyl nodes. (**B**) Same as panel (A) but with the lattice constants c = 1.401 nm in Ref. (*53*). Under this condition, WTe₂ is a Weyl semimetal. The conduction and valence band cross and form Weyl nodes. (**C**) A schematic showing the

momentum space distribution of the Weyl nodes in WTe$_2$. The dotted line shows the k-space cut for the dispersions shown in panels (A and B). (**D** and **E**) Surface Fermi surface calculations under the two lattice constant values. We see that the surface Fermi surfaces are extremely similar on a qualitative level. (**F**) ARPES measured Fermi surface on WTe$_2$, is consistent with the calculation in both panels (D and E). This shows that a qualitative agreement over the surface Fermi surface between calculation and ARPES does not prove Fermi arcs. (**G** and **H**) Surface state spin polarization calculations under the two lattice constant values. The color map shows the magnitude of the spin polarization. The arrows show the configuration of the spin texture. Although WTe$_2$ is trivial in panel (G) but Weyl semimetal in panel (H), the surface spin polarization and spin texture are extremely similar on a qualitative level.

(b) We show the calculated WTe$_2$ band structures with two slightly different lattice constant values according to two crystallographic studies (c=1.415 nm and c=1.401 nm (*53*, *54*)). For c = 1.415 nm (fig. S11**A**), we see that WTe$_2$ is trivial with no Weyl nodes. On the other hand, for c=1.401 nm (fig. S11**B**), WTe$_2$ becomes a Weyl semimetal. Now, figs. S11, **C** and **D** show the calculated surface state Fermi surfaces. Remarkably, although WTe$_2$ is trivial (without Weyl nodes) in one case but nontrivial (with Weyl nodes) in the other case, the surface Fermi surfaces are extremely similar on a qualitative level. This fact clearly demonstrates that an agreement between ARPES and calculations over the surface state Fermi surface does not unambiguously prove the Fermi arcs.

In fig. S11, **G** and **H**, we show the calculated surface state spin polarization of the two cases. We see that, the surface states show clear spin polarization regardless of the ground states, and their spin textures in figs. S11,**G** and **H** look very similar. Therefore, the surface state spin polarization also cannot be regarded as a decisive proof of the existence of topological Fermi arcs.

We note that although the example in fig. S11 is about WTe$_2$, the conclusion is applicable to other composition x of the W$_{1-x}$Mo$_x$Te$_2$ system. For any given composition, the W$_{1-x}$Mo$_x$Te$_2$ system can be tuned between the fully gapped trivial phase and the Weyl semimetal phase by changing its lattice constant c. Similarly, one will find that the surface Fermi surfaces of that composition are very similar at a qualitative level. Hence the data-calculation agreement on the surface Fermi surface cannot prove the existence of Fermi arcs for any composition of the W$_{1-x}$Mo$_x$Te$_2$ system.

(5) A detailed analysis of the W$_{1-x}$Mo$_x$Te$_2$ ARPES papers: Why these papers do not experimentally demonstrate the type-II Weyl fermions.

Here we provide a detailed analysis for why the W$_{1-x}$Mo$_x$Te$_2$ ARPES papers (32–38) do not show the type-II Weyl fermions and the type-II Weyl semimetal state.

1. W$_{1-x}$Mo$_x$Te$_2$ ARPES papers listed above tried to conclude Fermi arcs by showing a qualitative agreement between calculated and measured surface band structure. As we have shown above in figs. S10 and S11, such a method is not reliable. Moreover, the existence of Fermi arcs cannot distinguish between the type-I and type-II Weyl fermions.

2. Ref. (*36*) presented spin polarization measurements, which showed that the surface states are spin polarized. However, as we have shown above, the spin polarization and the spin texture are not a unique and unambiguous signature of the Fermi arcs (see fig. S11). Therefore, showing the surface spin polarization does not prove the existence of Fermi arcs. Moreover, the existence of Fermi arcs and their spin textures cannot distinguish between the type-I and type-II Weyl fermions.

3. Refs. (*32*, *37*) showed laser ARPES data ($h\nu \approx 6$ eV). The authors claimed that these data are in agreement with the type-II Weyl crossings. However, we emphasize that these data are significantly insufficient for an experimental demonstration of the type-II Weyl fermions, for the following important reasons:

3.1. In both works, the authors used a low and fixed photon energy ($h\nu \approx 6.7$ eV in Ref. (*32*) and $h\nu \approx 6$ eV in Refs. (*37*)). The low photon energy is mostly surface sensitive. In terms of the bulk band, low photon energy can probe the projected bulk bands, meaning bulk bands that are integrated at all k_z values. We emphasize that this is a very serious issue for demonstrating Weyl fermions.

3.2. We further note that, in both works, even the evidence for the projected crossing is fairly weak. Since the projected crossings are above the Fermi level, in both works, the authors divided their data by the Fermi-Dirac distribution to try to access above the Fermi level. However, this method makes the data significantly noisier. The data were marked by guides to the eye. Judging from the data quality, a clear projected crossing cannot be concluded by the data alone without the guides to the eye.

In fig. S12, we show a side-by-side comparison of some main data-figures between our work and the two $W_{1-x}Mo_xTe_2$ works (*32*, *37*). Most crucially, the ARPES data on is $W_{1-x}Mo_xTe_2$ about a projected crossing in the projected band structure on surface. As explained above in fig. S6, a projected band crossing does not prove the existence of a true band crossing in bulk band structure. In addition, the difference in data quality can be seen clearly. This is because the projected crossings in $W_{1-x}Mo_xTe_2$ are above the Fermi level and can only be accessed by normalizing the ARPES data by the Fermi-Dirac distribution. As seen from panels (**B** and **C**), the signals above the Fermi level are noisy. It is difficult and unreliable to draw conclusions based on the data alone without guides to the eye.
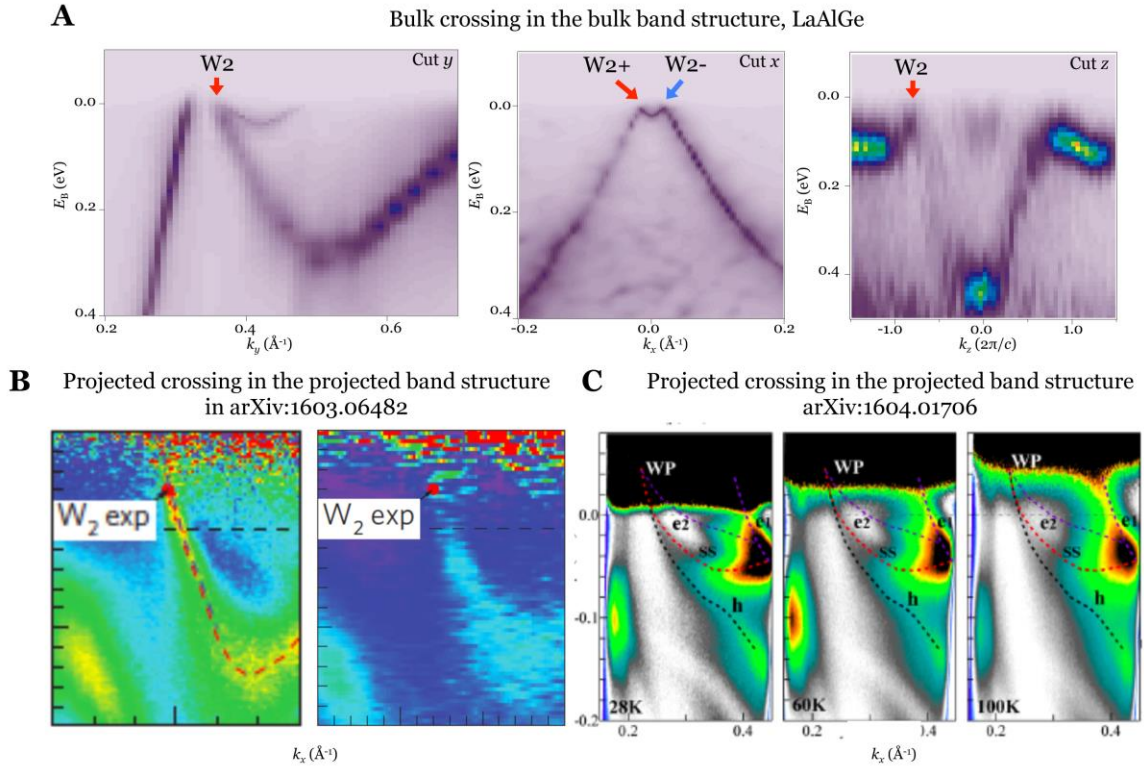
fig. S12. A side-by-side comparison of the main data figures between our work and the two
$W_{1-x}Mo_xTe_2$ works (*32, 37*). Most crucially, the ARPES data on is $W_{1-x}Mo_xTe_2$ about a projected
crossing in the projected band structure on surface. As explained above in fig. S6, a projected
band crossing does not prove the existence of a true band crossing in bulk band structure. In
addition, the difference in data quality can be seen clearly. This is because the projected crossings
in $W_{1-x}Mo_xTe_2$ are above the Fermi level and can only be accessed by normalizing the ARPES
data by the Fermi-Dirac distribution. As it can be seen in panels (**B** and **C**), the signals above the
Fermi level are noisy. It is difficult and unreliable to draw conclusions based on the data alone
without guides to the eye. By contrast, only in our work, we directly measure the bulk band
structure (with resolution) rather than their projections on the surface (without k_z resolution) and
show that the two bands disperse linearly away from the crossing along all three directions, k_x,
k_y and k_z, which unambiguously and conclusively shows that the observed crossing is a true
crossing point in the bulk band structure, a Weyl node.

section S6. Surface-state band structure of LaAlGe

We present the surface state band structure data measured by low-photon-energy ARPES in fig. S13.

Figure S13B shows the measured Fermi surface and constant energy contour data at different binding energies of the (001) surface. We identify the following features in the Fermi surface: (1) We observe a big contour centered at the $\overline{\Gamma}$ point; (2) We observe a tadpole-shaped feature along each $\overline{\Gamma} - \overline{X}(\overline{Y})$ line. The head of the tadpole along the $\overline{\Gamma} - \overline{X}$ direction is truncated by the big circle at the center; (3) We observe two small circular contours in the vicinity of each $\overline{X}$ point; (4) We observe an extended butterfly-shaped contour centered at the $\overline{Y}$ point. We find a reasonably good agreement between the ARPES measured (fig. S13B) and the calculated Fermi surfaces (fig. S13A) Specifically, all the features found in the ARPES data are also seen in the calculation. We note that all features in calculations contain weakly-split double contours, but in ARPES the linewidth of the measured bands is not sharp enough to resolve the splitting.
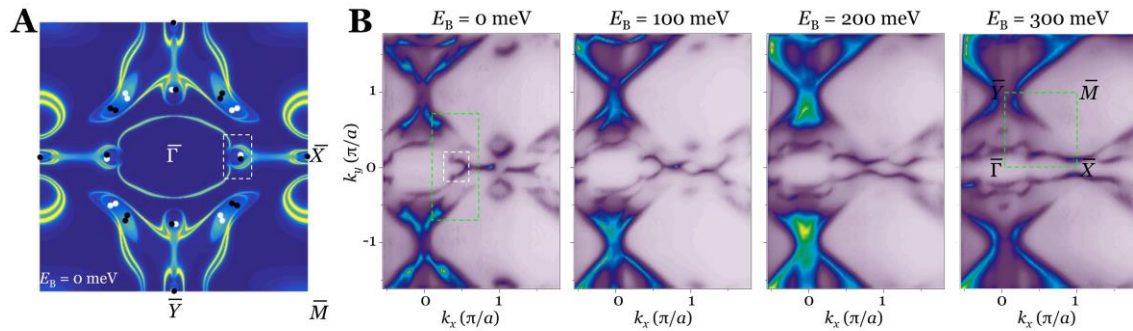

fig. S13. Fermi arc–like and Fermi arc–derived surface states in LaAlGe. (A) First-principles calculated $k_x - k_y$ Fermi surface map of the (001) surface. (**B**) ARPES-measured $k_x - k_y$ Fermi surface map and three different constant binding energy contours at $100\ meV$, $200\ meV$, and $300\ meV$ below the Fermi level measured with a photon energy of $50\ eV$.

section S7. Fermi arc surface states associated with the W$_2$ Weyl nodes in LaAlGe
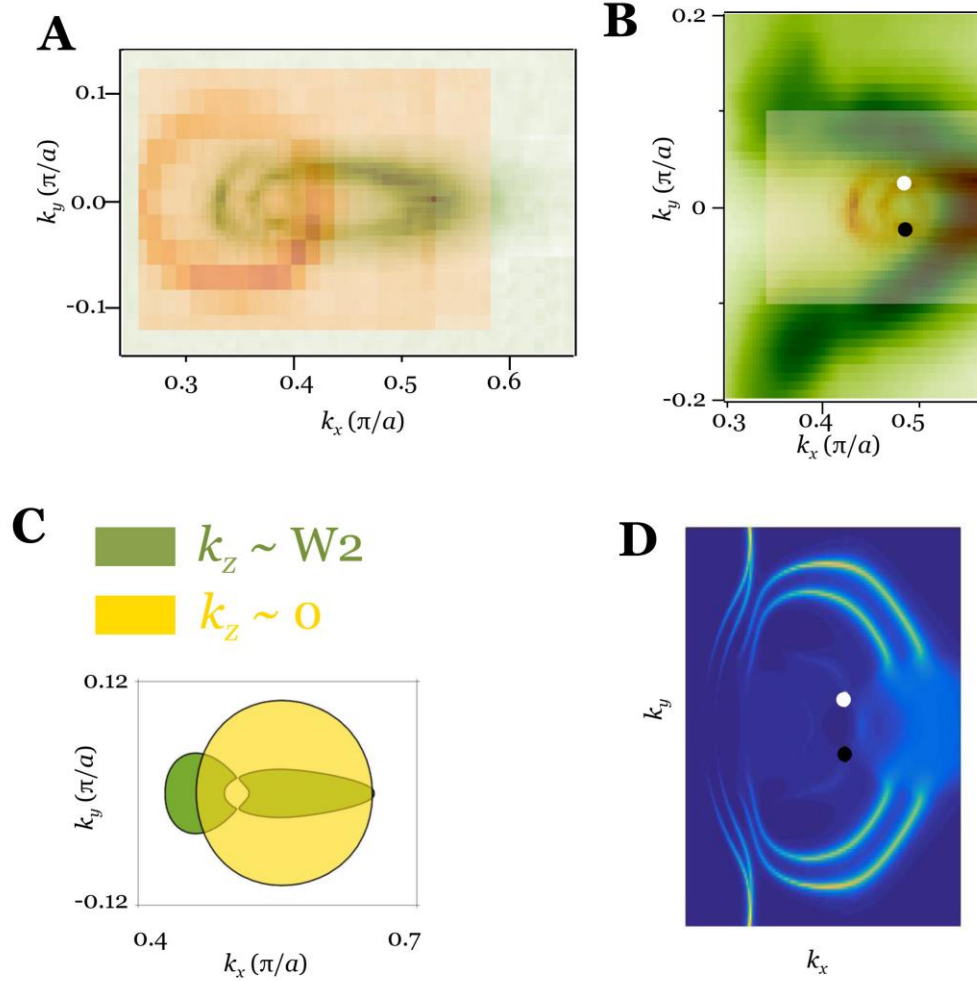

fig. S14. Fermi arc–like and Fermi arc–derived surface states in LaAlGe. (**A** and **C**) ARPES measured and theoretically calculated projected bulk Fermi surface near a pair of W$_2$ Weyl nodes. Both show that the W$_2$ Weyl nodes are masked by the irrelevant pockets when projected onto the surface. (**B**) ARPES surface Fermi surface map (the green color plot) with the bulk Fermi surface map (the orange color plot) overlaid on top of it to scale. (**D**) Theoretically calculated surface Fermi surface map near the W2 Weyl nodes.

As we have explained above, the existence/observability of the Fermi arcs associated with the W$_2$ Weyl nodes is ill-defined. Here we present the following data and calculations related to this point. From the ARPES data, we can learn the following:

(1) In the projected bulk band structure, the W$_2$ Weyl nodes are masked by the irrelevant pocket (fig. S14A). In fig. S14A, we superimpose the irrelevant bulk Fermi surface at $k_z = 0$ (the orange

color plot) onto the bulk Fermi surface at k_z =W$_2$ (the green color plot). We see that the W2 Weyl nodes are indeed masked by the irrelevant bulk Fermi surface at $k_z = 0$. This data proves that the existence/observability of the Fermi arcs associated with the W2 Weyl nodes is ill-defined, as we have emphasized above.

(2) The tadpole-shaped surface states do not go through the projected W2 nodes. In fig. S14B, we superimpose the bulk Fermi surface at k_z =W$_2$ (the orange color plot) onto the surface Fermi surface (the green color plot).

From the calculation, we can learn the following:

(1) In the projected bulk band structure, the W$_2$ Weyl nodes are masked by the irrelevant pocket.

(2) The tadpole-shaped surface states do not go through the projected W$_2$ nodes.

(3) Inside the head of the tadpole feature, we see very faint features in close vicinity of the W$_2$ nodes. These features are weak because they overlap with projected bulk bands. Precisely speaking, at the k points where the faint feature exists, the projected bulk band does not have a band gap (due to the irrelevant bulk band). At the top surface, their spectral weight is very small. Their spectral weight is mainly localized at the second unit cell or deeper away from the surface (15 A away from the top surface).

(4) We cannot define these faint features as surface states because of the lack of a projected band gap. For the same reason, we cannot demonstrate the existence of Fermi arcs.

section S8. Fermi arc surface states associated with the W₃′ and W₃″ Weyl nodes
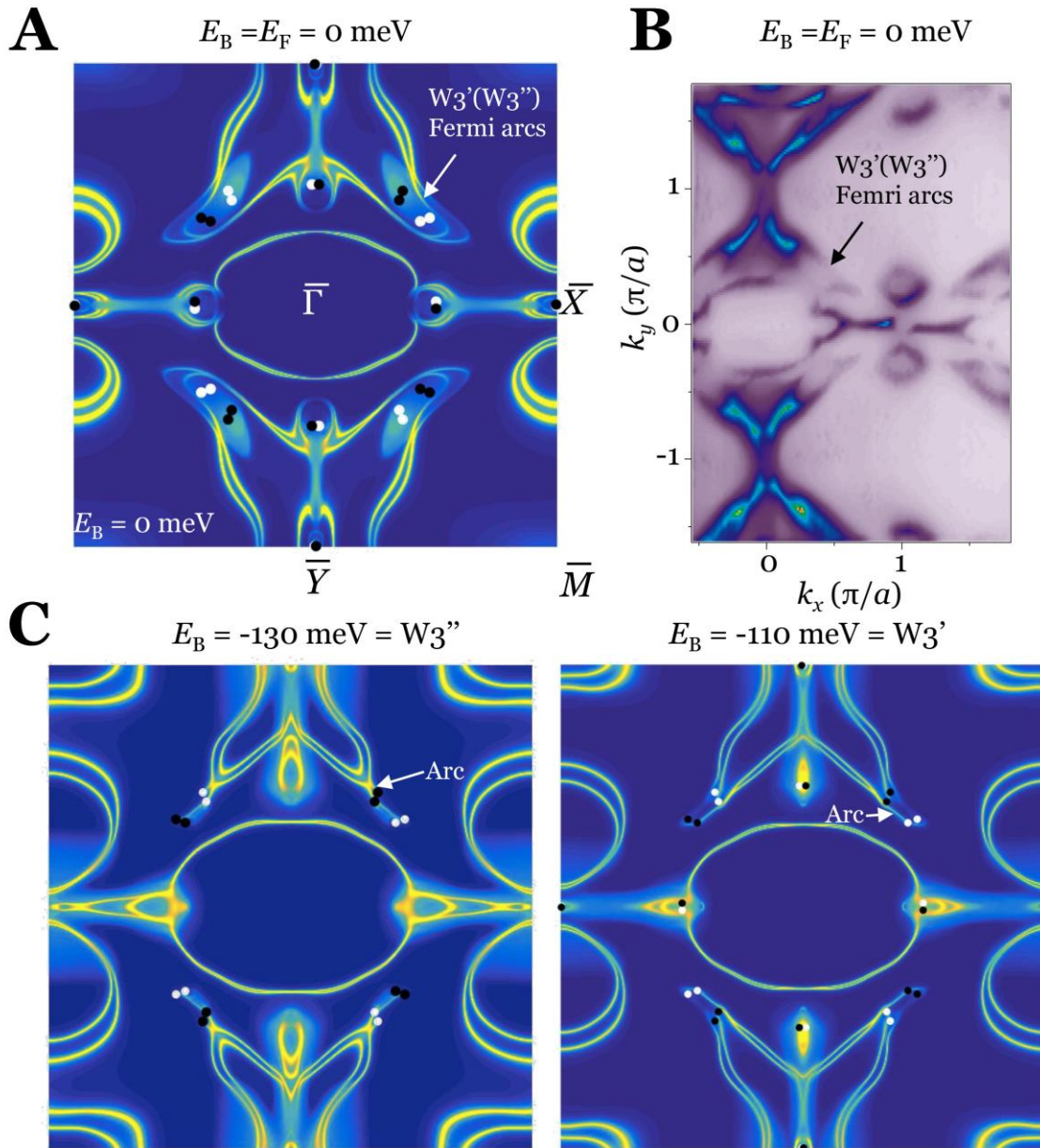

A $E_B = E_F = 0$ meV

W3'(W3")
Fermi arcs

$\overline{\Gamma}$

$\overline{X}$

$E_B = 0$ meV

$\overline{Y}$

$\overline{M}$

B $E_B = E_F = 0$ meV

W3'(W3")
Femri arcs

k_y (π/a)

k_x (π/a)

C $E_B = -130$ meV $= W3$"

Arc

$E_B = -110$ meV $= W3$'

Arc

fig. S15. Fermi arc surface states associated with the W₃′ and W₃″ Weyl nodes. (**A**) First-principles calculated surface Fermi surface ($E_B = E_F = 0\ meV$). The arrow points to the butterfly-shaped surface states, which corresponds to the Fermi arc surface states associated with the W3' and W3" Weyl nodes. (**B**) ARPES measured surface Fermi surface ($E_B = E_F = 0\ meV$). The arrow points to the butterfly-shaped surface states, which corresponds to the Fermi arc surface states associated with the W3' and W3" Weyl nodes. (**C and D**) First-principles calculated

surface constant energy contour at the energy of the W3" Weyl node, $E_B = -130\ meV$ (above the E_F).

A E_B = -130 meV = W3"

B Fermi arc connectivity at E = W3"

C E_B = -110 meV = W3"

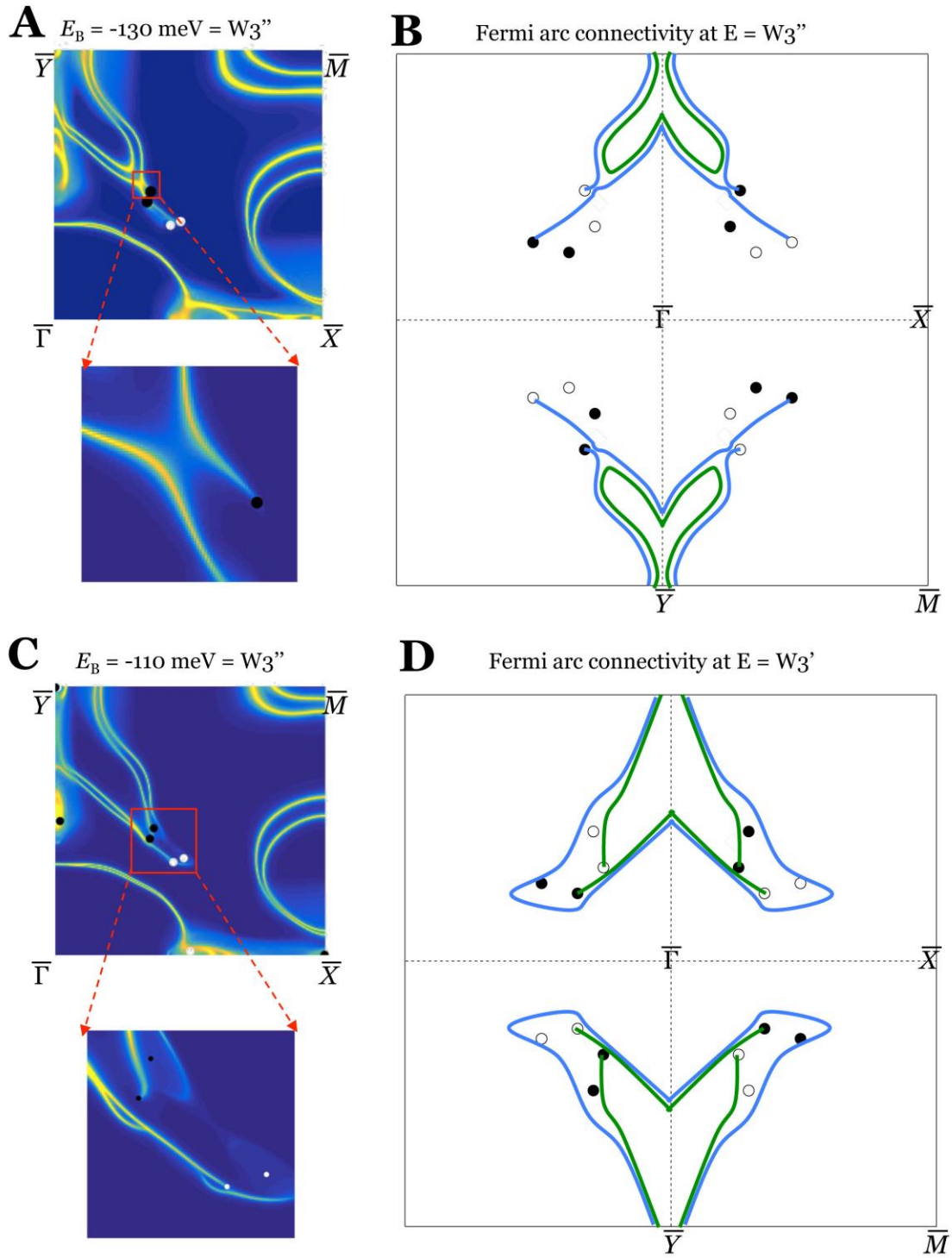**D** Fermi arc connectivity at E = W3'

fig. S16. Connectivity pattern of the Fermi arcs associated with the W₃′ and W₃″ Weyl nodes. (**A**) First-principles calculated surface constant energy contour at the energy of the W3"

Weyl node, $E_B = -130\ meV$ (above the E_F). (**B**) Schematic illustration of the Fermi arc connectivity for the W3'' Weyl nodes. The blue and green lines represent the outer and inner contour of the butterfly feature according to the calculation in panel (A). (**C** and **D**) Same as panels (A, B) but at the energy of the W3' Weyl node.

We show the existence of Fermi arc surface states associated with the W_3' and the W_3'' Weyl nodes based on the agreement between our ARPES data and calculations. Figure S15B shows the ARPES measured surface Fermi surface ($E_B = E_B = 0\ meV$). The arrow points to the butterfly-shaped surface states, which corresponds to the Fermi arc surface states associated with the W_3' and W_3'' Weyl nodes. The same feature was also found in the calculated surface Fermi surface (fig. S15A). In calculation, we know that the butterfly-shaped surface states are Fermi arcs. This is achieved by calculating the surface band structure directly at the energies of the W_3' and W_3'' Weyl nodes, which are 110 meV and 130 meV above the Fermi level, respectively, as shown in figs. S15, C and D and fig. S16. Because our ARPES data and calculations agree with each other on the butterfly-shaped surface states at energies below the Fermi level and because from our calculation we know that the butterfly-shaped surface states are indeed the Fermi arcs (the actual arc behavior happens above the Fermi level because the $W_3'(W_3'')$ Weyl nodes are above the Fermi level), we show the existence of Fermi arc surface states associated with the W_3' and the W_3'' Weyl nodes.

We note that the degree of robustness of this demonstration is the same as the ARPES works claiming observations of Fermi arcs in the $W_{1-x}Mo_xTe_2$ systems (32‑38) because the conclusion is drawn based on the agreement between data and calculations. Note that in both cases, the actual arc behavior happens above the Fermi level because the Weyl nodes are above the Fermi level. In our case, the $W_3'(W_3'')$ Weyl nodes are $\sim 110\ meV$ and $130\ meV$ above the Fermi level, respectively. In $W_{1-x}Mo_xTe_2$, the Weyl nodes are $50\ meV$ above the Fermi level.

section S9. Topological definition of Fermi arc surface states and its implications for surface states in LaAlGe and $W_{1-x}Mo_xTe_2$

We elaborate on why the type-II Weyl fermions in LaAlGe dominate the Berry curvature physics at the Fermi level. The Weyl (Berry curvature) physics include the negative longitudinal magneto-resistance due to the chiral anomaly, the nonlocal transport due to the chiral anomaly.

The Fermi surface of LaAlGe consists of (1) the type-II Weyl nodes are at the Fermi level with their associated electron and hole pockets, (2) the pockets arising from the other Weyl fermion cones whose Weyl node energies are far away from the Fermi level, and (3) irrelevant pockets. The Berry curvature at the Fermi level is truly dominated by the type-II Weyl nodes are at the Fermi level because Weyl nodes are Berry curvature monopoles.

To demonstrate this point more quantitatively, in Fig. 4 of the main text, we have shown the calculated Berry curvature of the LaAlGe band structure. The color plots in figs. 4B and C show the Berry curvature magnitude in k_x, k_y space at the two different k_z values. We note that figs. 4B and C consider the Berry curvature magnitude summed over contributions from a wide energy range. It can be seen that the Berry curvature is indeed dominated by the contribution from the Weyl nodes. By contrast, the trivial pocket at $k_z = 0$ has no observable Berry curvature contribution. In order to understand the low-energy Berry curvature physics, which can be measured by certain transport experiments such as the negative longitudinal magneto-resistance, we need to know the Berry curvature in close vicinity of the Fermi energy. In figs. 4E and F, we show the Berry curvature magnitude again but only considering the contribution near the Fermi level within a ± 10 meV window. We see that the Fermi pockets that arise from W1 and $W_3'(W_3'')$ Weyl cones (Fig. 4E) do not carry observable Berry curvature. On the other hand, Fermi pockets that arise from the type-II Weyl cones (Fig. 4E) show strong Berry curvature in the vicinity of the W_2 Weyl nodes. This is quite intuitive. Since the Weyl nodes are monopoles, the Berry curvature decays rapidly as $1/E^2$ away from the energy of the node. Therefore, the Fermi pockets from W1 and $W_3'(W_3'')$ Weyl cones show negligiblely small Berry curvature contribution. We prove that the type-II Weyl nodes dominate the low-energy Berry curvature physics, which dictates topological phenomena such as the negative longitudinal magneto-resistance and the nonlocal transport due to the chiral anomaly (*10*, *11*).